

Journal of Biomedical Optics

SPIEDigitalLibrary.org/jbo

Reconstruction of fluorescence molecular tomography via a nonmonotone spectral projected gradient pursuit method

Jinzuo Ye
Yang Du
Yu An
Chongwei Chi
Jie Tian

Reconstruction of fluorescence molecular tomography via a nonmonotone spectral projected gradient pursuit method

Jinzuo Ye,^a Yang Du,^a Yu An,^b Chongwei Chi,^{a,*} and Jie Tian^{a,*}

^aChinese Academy of Sciences, Key Laboratory of Molecular Imaging of Chinese Academy of Sciences, Institute of Automation, No.95 Zhongguancun East Road, Haidian District, Beijing 100190, China

^bBeijing Jiaotong University, School of Computer and Information Technology, Department of Biomedical Engineering, No.3 Shangyuan, Haidian District, Beijing 100044, China

Abstract. Fluorescence molecular tomography (FMT) is a promising imaging technique in preclinical research, enabling three-dimensional location of the specific tumor position for small animal imaging. However, FMT presents a challenging inverse problem that is quite ill-posed and ill-conditioned. Thus, the reconstruction of FMT faces various challenges in its robustness and efficiency. We present an FMT reconstruction method based on nonmonotone spectral projected gradient pursuit (NSPGP) with l_1 -norm optimization. At each iteration, a spectral gradient-projection method approximately minimizes a least-squares problem with an explicit one-norm constraint. A nonmonotone line search strategy is utilized to get the appropriate updating direction, which guarantees global convergence. Additionally, the Barzilai–Borwein step length is applied to build the optimal step length, further improving the convergence speed of the proposed method. Several numerical simulation studies, including multisource cases as well as comparative analyses, have been performed to evaluate the performance of the proposed method. The results indicate that the proposed NSPGP method is able to ensure the accuracy, robustness, and efficiency of FMT reconstruction. Furthermore, an *in vivo* experiment based on a heterogeneous mouse model was conducted, and the results demonstrated that the proposed method held the potential for practical applications of FMT. © 2014 Society of Photo-Optical Instrumentation Engineers (SPIE) [DOI: [10.1117/1.JBO.19.12.126013](https://doi.org/10.1117/1.JBO.19.12.126013)]

Keywords: fluorescence molecular tomography; image reconstruction; inverse problems; nonmonotone spectral projected gradient pursuit; tumor detection; *in vivo* imaging.

Paper 140606R received Sep. 22, 2014; accepted for publication Nov. 18, 2014; published online Dec. 24, 2014.

1 Introduction

Optical molecular imaging (OMI) techniques have played an increasingly important role in revealing the dynamic interactions of biological processes at cellular and molecular levels.^{1–4} As one of the various modalities of OMI, fluorescence molecular imaging (FMI) has received particular attention because of its high resolution and sensitivity.⁵ By using an ultrasensitive charge-coupled device (CCD) camera to detect the fluorescence emitted by living tissues with fluorescent probes, FMI allows researchers to monitor cell growth and localize tumors *in vivo*. Recently, fluorescence molecular tomography (FMT) can three-dimensionally detect the unknown biodistribution of fluorescent probes inside biological tissues, thus greatly facilitating its applications in small animal research and preclinical diagnostics.^{6–8}

One of the challenging problems for FMT is the highly ill-posed inverse problem due to the multiple scattering and potential absorption of photons propagating through heterogeneous biological tissues.^{7,9} Besides, the only measurable information for the FMT reconstruction is the two-dimensional photon distribution on the boundary of the target; this situation can be alleviated by using the free-space and multiprojection strategies based on the noncontact full angle FMT imaging system to acquire more measurement data sets.¹⁰ However, even if

sufficient measurements can be obtained, the FMT problem may still be ill-conditioned because it is very sensitive to noise caused by CCD measurement errors and data discretization errors. Furthermore, high sampling measurements and real animal-shape geometry modeling usually lead to a large weight matrix, which results in an inherently large computational burden for the FMT inverse problem. Therefore, FMT reconstruction faces various challenges in efficiency and robustness, and the development of feasible FMT reconstruction methods is important for the achievement of practical biomedical applications.

Over the past few years, extensive work aimed at solving the challenging FMT inverse problem has been performed. Researchers have proposed various regularization methods to make the solution stable and insensitive to noise. Tikhonov regularization has been widely adopted in resolving FMT and other optical tomographic problems.^{11–14} This regularization method adds the l_2 -norm constraint of the solution to the original problem, thus making the solution less sensitive to perturbations. The primary benefit of using Tikhonov regularization is that the optimization problem is simple and can be efficiently solved by standard minimization tools, such as the Newton method and the conjugate gradient method. However, the Tikhonov method may result in an oversmoothed solution and lose some localized features during reconstruction.¹⁵

*Address all correspondence to: Chongwei Chi and Jie Tian, E-mail: chichongwei@fingerpass.net.cn and tian@iee.org

Sparsity regularization, which is widely used in the field of compressed sensing (CS), has been incorporated in optical tomographic problems to promote the sparsity of the solution in recent years.^{16,17} Guided by the CS theory, a sparse or compressive signal can be faithfully recovered from far fewer samples or measurements.^{18,19} For FMT, fluorescent signals usually have a similar property of sparse signals based on the fact that the domains of the fluorescent sources are small and sparse compared with the entire reconstruction domain, because the size of early-stage tumors tagged with the fluorescent probes is small.²⁰ The advantage of using sparsity regularization is that it can still perform well when the measurement data sets are very limited. In recent years, inspired by the ideas behind the CS theory, various algorithms incorporated with l_1 -norm regularization have been proposed to solve optical tomography problems,^{21–25} such as the iterated shrinkage based method with l_1 -norm (IS_L1) and the stagewise orthogonal matching pursuit based method.

Although there are many challenging problems in FMT reconstruction, consistent efforts are still being made to develop more feasible reconstruction methods combined with *a priori* knowledge for a more practical application. In this paper, we demonstrated an efficient method using the nonmonotone spectral projected gradient pursuit (NSPGP) with l_1 -norm optimization, while taking *a priori* structural information to localize the fluorescent signals. The classical spectral projected gradient method is utilized to minimize a least-squares problem with an explicit one-norm constraint. A nonmonotone line search strategy is adopted to get the appropriate updating direction, which guarantees global convergence. Moreover, the spectral step length, which was introduced by Barzilai and Borwein²⁶ and analyzed by Raydan,²⁷ is utilized to build the optimal step length, further accelerating the convergence process of the proposed NSPGP method. To evaluate the performance of the proposed method, numerical simulation studies, including multisource cases as well as comparative analyses, have been performed. The results suggested that the proposed NSPGP method was more accurate, efficient, and robust for fluorescence reconstruction compared to contrasting methods. Furthermore, an *in vivo* experiment based on a heterogeneous mouse model was conducted, and the results demonstrated that the proposed method held the potential for practical applications of FMT.

In Sec. 2, we present the reconstruction methodology for FMT. In Sec. 3, numerical simulation experiments of the proposed method are conducted. In Sec. 4, an *in vivo* experiment based on a heterogeneous mouse model further demonstrates the reliability of the proposed method. In Sec. 5, we discuss relative issues and conclude our work.

2 Materials and Methods

2.1 Photon Propagation Model

For photon propagation in biological tissues within the near-infrared spectral window, scattering is the dominant phenomenon over absorption. Therefore, the diffusion equation is usually used to model photon transport in highly scattering media.^{28,29} For steady-state FMT with point excitation sources, the forward problem of photon propagation can be modeled as the following coupled diffusion equations:³⁰

$$\begin{cases} \nabla \cdot [D_x(r) \nabla \Phi_x(r)] - \mu_{ax}(r) \Phi_x(r) = -\Theta \delta(r - r_l) \\ \nabla \cdot [D_m(r) \nabla \Phi_m(r)] - \mu_{am}(r) \Phi_m(r) = -\Phi_x(r) \eta \mu_{af}(r) \end{cases} \quad (r \in \Omega), \quad (1)$$

where subscripts x and m denote the excitation and emission wavelengths, respectively; Ω denotes the domain of the problem; $\Phi_{x,m}$ is the photon flux density for excitation (subscript x) and emission (subscript m); $\mu_{ax,am}$ is the absorption coefficient; $D_{x,m} = 1/3[\mu_{ax,am} + (1-g)\mu_{sx,sm}]$ is the diffusion coefficient, where $\mu_{sx,sm}$ is the scattering coefficient and g is the anisotropy parameter; and $\eta \mu_{af}$ is the unknown fluorescent yield to be reconstructed, which incorporates the quantum efficiency η and absorption coefficient μ_{af} of the fluorescent probe. In the forward model, the excitation light is implemented as the isotropic point source $\Theta \delta(r - r_l)$, which is located one mean free path of photon transport beneath the surface. Θ is the amplitude of the point source and $\delta(r)$ is the Dirac function.

To solve the coupled equations, the Robin-type boundary conditions are implemented on the boundary $\partial\Omega$ of domain Ω :³¹

$$2D_{x,m}(r) \partial \Phi_{x,m}(r) / \partial \vec{n}(r) + q \Phi_{x,m}(r) = 0 \quad (r \in \partial\Omega), \quad (2)$$

where \vec{n} is the outward normal vector to the surface $\partial\Omega$ and q is a constant, which is approximated as $q \approx (1+R)/(1-R)$. R is a parameter governing the internal reflection at the boundary $\partial\Omega$.

2.2 Linear Relationship Establishment

The finite element method is applied to solve the diffusion equations [Eq. (1)] together with the boundary condition [Eq. (2)]. The domain is discretized with tetrahedrons and the base functions are taken as the test functions. Then the FMT problem can be linearized and the following matrix-form equations can be obtained:

$$[K_x] \{\Phi_x\} = \{S_x\}, \quad (3)$$

$$[K_m] \{\Phi_m\} = [D] \{X\}, \quad (4)$$

with $D(i, j) = \int_{\Omega} \Phi_x(r) \psi_i(r) \psi_j(r) dr$, where $\Psi_i(r)$ and $\Psi_j(r)$ denote the base function of node i and node j , respectively; K_x and K_m denote the system matrix during excitation and emission, respectively; S_x denotes the excitation source distribution after discretization; matrix F is obtained by discretizing the unknown fluorescent yield distribution; and vector X denotes the fluorescent yield to be reconstructed.

Photon density Φ_x , which is used as the energy source for the emission process, can be obtained by solving Eq. (3). Considering the inverse crime problem, Φ_x is calculated on a fine mesh using second-order Lagrange elements. Then, it is projected onto a coarse mesh, which will be used for the reconstruction of X with linear elements. Considering that K_m is symmetrical and a positive definite, Eq. (4) can be transformed into the following matrix-form equation:

$$\{\Phi_{m,l}\} = [K_{m,l}^{-1}] [D_l] \{X\} = [F_l] \{X\}. \quad (5)$$

By removing the immeasurable entries in $\Phi_{m,l}$ and the corresponding rows in F_l , we have

$$\{\Phi_{m,l}^{meas}\} = [A_l]\{X\}. \quad (6)$$

Next, Eq. (6) for different excitation locations is assembled and the following matrix-form equation is obtained:

$$\{\Phi\} = [A]\{X\}. \quad (7)$$

Hence, the procedure to solve the diffusion equations has been simplified into the form of linear equations, which can improve computational efficiency. It is worth mentioning that Eq. (7) is an underdetermined system of linear equations with fewer equations than unknowns because the surface photon density distribution is far more limited than the unknown internal fluorescence density distribution, consequently causing difficulties in the following three-dimensional (3-D) reconstruction.

2.3 Reconstruction Based on Nonmonotone Spectral Projected Gradient Pursuit

As mentioned above, the domains of the fluorescent sources are small and sparse compared with the entire reconstruction domain. This can be regarded as a kind of *a priori* information of the fluorescent sources. Here, l_1 regularization is adopted in the FMT problem to promote the sparsity of the solution. In this case, Eq. (7) can be transformed into the following one-norm regularized least-squares problem:

$$\underset{x}{\text{minimize}} E(x) = \frac{1}{2} \|Ax - \Phi\|_2^2 + \lambda \|x\|_1, \quad (8)$$

where λ is the regularization parameter for Eq. (8). Another statement of the one-norm regularized least-squares problem has the following form:

$$\underset{x}{\text{minimize}} f(x) = \|Ax - \Phi\|_2^2 \quad \text{subject to } \|x\|_1 \leq \tau, \quad (9)$$

which has an explicit one-norm constraint and is often called the Lasso problem.³² τ denotes the regularization parameter that is used to govern the sparsity of the solution. $f(x) = Ax - \Phi_2^2$ denotes the objective function.

To find the best sparse solution that stands for the fluorescent sources, a novel method named the NSPGP method, will be introduced in this section to solve Eq. (9). In the NSPGP method, the classical projected gradient scheme is extended to include a nonmonotone step length strategy based on a nonmonotone line search. The nonmonotone line search strategy is applied to allow the overall convergence. To speed up the convergence of the NSPGP method, the Barzilai–Borwein step length (also known as the spectral step length) is adopted in this method, which only requires a little computational work. To the best of our knowledge, the spectral projected gradient method has rarely been used in FMT. The main steps of the proposed NSPGP method are summarized below:

To further illustrate how such a method fits into FMT reconstruction, we mathematically derived the NSPGP method using the following steps.

Step 1—to project iterates onto the feasible set by one-norm projection: The NSPGP method depends on the ability to project iterates onto the feasible set $\{x | x_1 \leq \tau\}$. This is accomplished via a projection operator defined as

Algorithm 1 Nonmonotone Spectral Projected Gradient Pursuit.

Input:

Matrix A , vector Φ , threshold parameter σ . The maximum number of iterations N_{\max}

Initialization:

The initial regularization parameter τ .

The minimum and maximum step lengths $0 < \alpha_{\min} < \alpha_{\max}$.

The initial step length $\alpha_0 \in [\alpha_{\min}, \alpha_{\max}]$.

The sufficient descent parameter $\gamma \in (0, 1)$.

The line search history length $L > 1$.

$$x_0 = P_\tau[x], r_0 = \Phi - Ax_0, g_0 = -A^T r_0.$$

$$n = 1$$

Iteration ($n \geq 1$):

$$(1) \quad \alpha = \alpha_{n-1}$$

Internal Iteration:

$$(2) \quad x_n = P_\tau(x_{n-1} - \alpha g_{n-1})$$

$$(3) \quad r_n = \Phi - Ax_n$$

$$(4) \quad d_n = x_n - x_{n-1}$$

$$(5) \quad \text{if } \|r_n\|_2^2 \leq \max_{0 \leq j \leq \min(n-1, L-1)} \|r_{n-1-j}\|_2^2 + \gamma (d_n)^T g_{n-1} \text{ then}$$

$$(6) \quad \text{Exit internal iteration}$$

else

$$(7) \quad \alpha = \alpha/2$$

end if

End Internal Iteration

$$(8) \quad g_n = -A^T r_n$$

$$(9) \quad \Delta x = x_n - x_{n-1}; \Delta g = g_n - g_{n-1}$$

$$(10) \quad \alpha_{BB} = (\Delta x^T \Delta x) / (\Delta x^T \Delta g)$$

$$(11) \quad \text{if } \Delta x^T \Delta g \leq 0 \text{ then}$$

$$(12) \quad \alpha_n = \alpha_{\max}$$

Else

$$(13) \quad \alpha_n = \min\{\alpha_{\min}, \max[\alpha_{\min}, \alpha_{BB}]\}$$

end if

$$(14) \quad n = n + 1$$

$$(15) \quad \text{if halting condition true (i.e., } r_n < \sigma \text{ or } n > N_{\max}\text{), then quit the iteration, End if}$$

End Iteration

Output:

$$(16) \quad x = x_n$$

$$P_\tau(c) = \underset{x}{\operatorname{argmin}} \|c - x\|_2 \quad \text{subject to } \|x\|_1 \leq \tau. \quad (10)$$

This projection operator gives a vector c onto the one-norm ball with radius τ . In this step, the projection $P_\tau(\cdot)$ of a candidate iterate is computed to get the newly estimated solution $x_n = P_\tau(x_{n-1} - \alpha g_{n-1})$ of the FMT problem, where g_{n-1} is the gradient [for the objective function $f(x) = Ax - \Phi_2^2$] generated in the previous iteration. The newly estimated residual r_n and the search direction d_n are then calculated.

Step 2—to obtain the step length α and to re-evaluate the newly generated solution x_n : the residual r_n and the search direction d_n are found by a nonmonotone line search strategy. The criterion used in the internal iteration results in a nonmonotone line search:

$$\|r_n\|_2^2 \leq \max_{0 \leq j \leq \min(n-1, L-1)} \|r_{n-1-j}\|_2^2 + \gamma(d_n)^T g_{n-1}, \quad (11)$$

which ensures that at least every $L(L > 1)$ iteration yields a sufficient decrease in the objective function. It is worth mentioning that the residual r_n is equal to the objective function value $f(x_n)$ in the n 'th iteration. γ denotes the sufficient descent parameter. In obtaining a proper step length α , traditional line searches, such as the Armijo line search or the Wolfe line search, require the objective function value to decrease monotonically at every iteration, namely:

$$f(x_n) \leq f(x_{n-1}). \quad (12)$$

However, the nonmonotone line search strategy does not require the objective function value to decrease monotonically. Hence, it is helpful to overcome the case where the sequence of iterates follows the bottom of a curved narrow valley, which may occur in some difficult optimization problems.^{33,34} Therefore, global convergence is ensured by the monotone line search strategy, which forces the decrease of the objective function at each step.

Step 3—to generate the new step length by using the Barzilai–Borwein step length: The initial candidate iterate in the internal iteration (steps 2 to 7) is determined by the step length computed in steps 8 to 13. In order to compute the new step length α_n , which will be used in the next iteration, the Barzilai–Borwein step length is adopted. The Barzilai–Borwein step length, which was introduced by Barzilai and Borwein and analyzed by Raydan, is defined as follows:^{26,27}

$$\alpha_{BB} = (\Delta x^T \Delta x) / (\Delta x^T \Delta g), \quad (13)$$

where Δx is the increment of x_n between two iterations and Δg is the gradient increment of the objective function between two iterations. Then, the new step length used in the next iteration can be calculated by

$$\alpha_n = \min\{\alpha_{\max}, \max[\alpha_{\min}, \alpha_{BB}]\}, \quad (14)$$

where α_{BB} denotes the Barzilai–Borwein step length; $\alpha_{\min} = 10^{-10}$ and $\alpha_{\max} = 10^{10}$ are two initial parameters. The primary benefit of using the Barzilai–Borwein step length is that it requires little computational work and can greatly speed up the convergence of gradient methods.³⁵

Step 4—to determine whether or not it is time to discontinue the proposed NSPGP method: There are many halting conditions for practical FMT reconstruction methods, such as

when the norm of the residual is below a certain threshold or when the relative residual improvement between two consecutive iterations is below a certain threshold, because taking more costly iterations is not worth it if the resulting improvement is too small. In the proposed NSPGP method, we end the iteration when the residual r_n is smaller than a certain threshold σ or the maximum iteration number N_{\max} is reached. In the following experiments, the parameters σ and N_{\max} were optimized according to experimental experience. The parameter σ was set to $0.06 \cdot \operatorname{norm}(\Phi)$, where $\operatorname{norm}(\Phi)$ is the Euclidean length of vector Φ . In the following experiments, the reconstruction method was able to obtain satisfactory results when using $0.06 \cdot \operatorname{norm}(\Phi)$ as the value of parameter σ . The parameter N_{\max} was set to be 1000. In our experiments, all of the reconstructions with the proposed method stopped within 1000 iterations.

If the halting conditions are not satisfied, we set $n = n + 1$ and go to the next iteration. Otherwise, we output the final solution x , satisfying $x = x_n$.

The selection of a regularization parameter is still an open active research area for FMT. To our best knowledge, there is no efficient way to accurately select the optimal regularization parameter for each algorithm.³⁶ In this paper, the regularization parameter τ for the proposed method was manually optimized and was set to 0.8. In our experiments, it is good enough to obtain satisfactory results when using 0.8 as the regularization parameter.

3 Results and Discussion

In this section, both numerical simulation studies and *in vivo* mouse studies have been conducted to analyze the accuracy, efficiency, and robustness of the proposed method. All of the reconstructions were performed on our desktop computer with 2.39 GHz Intel Core 2 Duo CPU and 2 GB RAM.

3.1 Heterogeneous Mouse Model for Numerical Simulation Studies

Before reconstruction, the anatomical structure of the BALB/c mouse was developed using our micro-CT system and cone-beam reconstruction algorithm.^{37,38} Several primary organs were delineated by interactive segmentation methods to build the heterogeneous mouse model. Since the segmented organs are mainly in the mouse torso, this part was used for imaging reconstructions. The 3-D view of the heterogeneous mouse model is shown in Fig. 1(a), consisting of six kinds of materials to represent muscle, lungs, heart, kidneys, liver and bone. The optical parameters of different organs for both the excitation and emission wavelength are listed in Table 1.^{7,39,40} Figure 1(b) is the cross-section image of the mouse model in the $z = 0.02$ m plane. The black dots in Fig. 1(b) represent the excitation light sources, which were modeled as isotropic point sources located one mean free path beneath the surface in the $z = 0.02$ m plane. As mentioned above, the fluorescent sources are usually small and sparse for FMT, so small spheres with a diameter of 2 mm centered in the $z = 0.02$ m plane were used to represent the fluorescent sources. Figure 1(c) demonstrates the setup of the mouse model for triple fluorescent sources, and the liver region is set to be translucent so that the fluorescent sources are not covered. The fluorescent sources S1 and S2 are in the liver area and the fluorescent source S3 is in the muscle area, as shown in Figs. 1(c) and 1(d). The fluorescent yields of the sources were all set to be 0.3 mm^{-1} . Fluorescence measurement was implemented in the transillumination mode. For each

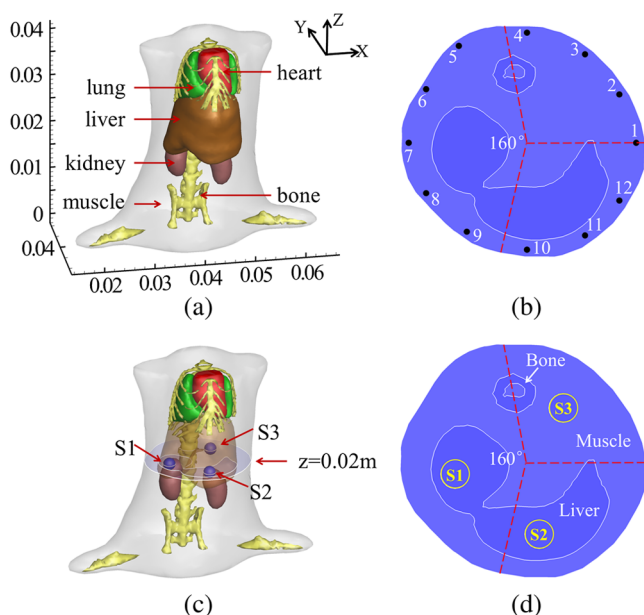


Fig. 1 The heterogeneous mouse model for numerical simulation studies. (a) Three-dimensional (3-D) view of the heterogeneous mouse model. (b) The cross-section image of the mouse model in the $z = 0.02$ m plane. (c) The setup of the mouse model for triple sources. (d) The cross-section image of the mouse model with triple fluorescent sources in the $z = 0.02$ m plane. S1, S2, and S3 denote the source number of the first source, the second source, and the third source, respectively.

excitation source, the emitted fluorescence was captured from the opposite side of the mouse model with a 160 deg field of view, as illustrated in Fig. 1(b). For practical FMT experiments using a CCD camera, the shot noise always exists and will approach a Gaussian distribution when large numbers of photons are collected. To simulate the real case, we added 5% Gaussian noise to the measurement data.

To better evaluate the proposed method, two other classical reconstruction algorithms were utilized to reconstruct the same data sets. One was IS_L1, which was proposed by Han et al.²³ The other was the conjugate gradient based method with the l_2 -norm (CG_L2).⁴¹ All of the reconstructions were conducted using MATLAB® on a desktop computer with 2.39 GHz Intel Core 2 Duo CPU and 2 GB RAM.

Table 1 Optical parameters of the heterogeneous model.

Material	μ_{ax} (mm ⁻¹)	μ'_{sx} (mm ⁻¹)	μ_{am} (mm ⁻¹)	μ'_{sm} (mm ⁻¹)
Muscle	0.0052	1.08	0.0068	1.03
Lungs	0.0133	1.97	0.0203	1.95
Heart	0.0083	1.01	0.0104	0.99
Liver	0.0329	0.70	0.0176	0.65
Kidneys	0.0660	2.25	0.0380	2.02
Bone	0.0024	1.75	0.0035	1.61

3.2 Evaluation of Reconstruction Accuracy

In the first experiment, we reconstructed the fluorescent sources to evaluate the reconstruction accuracy of the proposed method. Fluorescence was excited by point sources from 12 different locations in sequence, as illustrated in Fig. 1(b). Measurements of emission fluorescence were collected every 30 deg and a total number of 12 data sets were acquired for the reconstruction of the fluorescent sources. Figure 2 gives the reconstruction results from the CG_L2 method, the IS_L1 method, and the proposed method, demonstrating the 3-D views of the reconstructed sources in the heterogeneous mouse model and the slice images in the $z = 0.02$ m plane. The red circles in the slice images denote the real positions of the fluorescent sources. From Fig. 2 we can clearly see that the results from both the proposed method and the IS_L1 method are satisfactory. However, the results from the CG_L2 method were oversmoothed due to the oversmoothing effect of the Tikhonov regularization. The sizes of the reconstructed sources by the CG_L2 method were much larger than the actual sizes of the fluorescent sources, and the fluorescence reconstructed by the CG_L2 method had a low contrast to the background due to oversmoothing. To quantitatively analyze the results, we define the position error (PE) as

$$PE = \|L_r - L_a\|_2, \quad (15)$$

where L_a is the central position of the fluorescent source and L_r is the position of the finite element node with the maximum reconstructed value of the fluorescent yield for that source. We also define the relative intensity error (RIE) as

$$RIE = \frac{|I_r - I_a|}{I_a}, \quad (16)$$

where I_a denotes the actual fluorescent yield of the fluorescent source and I_r denotes the maximum fluorescent yield of the corresponding reconstructed source. The quantitative comparisons among the reconstruction results for 12 measurement data sets corrupted by 5% Gaussian noise are presented in Table 2. As shown in Table 2, the PEs by the proposed method and the IS_L1 method are the same and are smaller than those by the CG_L2 method. The RIEs by the proposed method are smaller than the CG_L2 method and the IS_L1 method; that is, the fluorescence reconstructed by the proposed method has higher contrasts compared with that of the other two methods.

3.3 Evaluation of Reconstruction Robustness of Limited Measurement Data

To further evaluate the reconstruction performance, robustness testing of limited measurement data sets was conducted for the proposed method. Usually, the tomographic imaging quality is sensitive to limited measurement data sets. In this experiment, we reduced the amount of the measurement data sets to simulate a much worse case scenario. This is quite necessary when long-term measurement is not feasible or is inappropriate. For example, when doing small animal noninvasive imaging, long-term measurement may cause the bleaching effect of the fluorescent probe, which has a direct effect on the reconstruction results. One way to resolve this problem is to reduce the number of measurement data sets. This requires us to be able to reconstruct

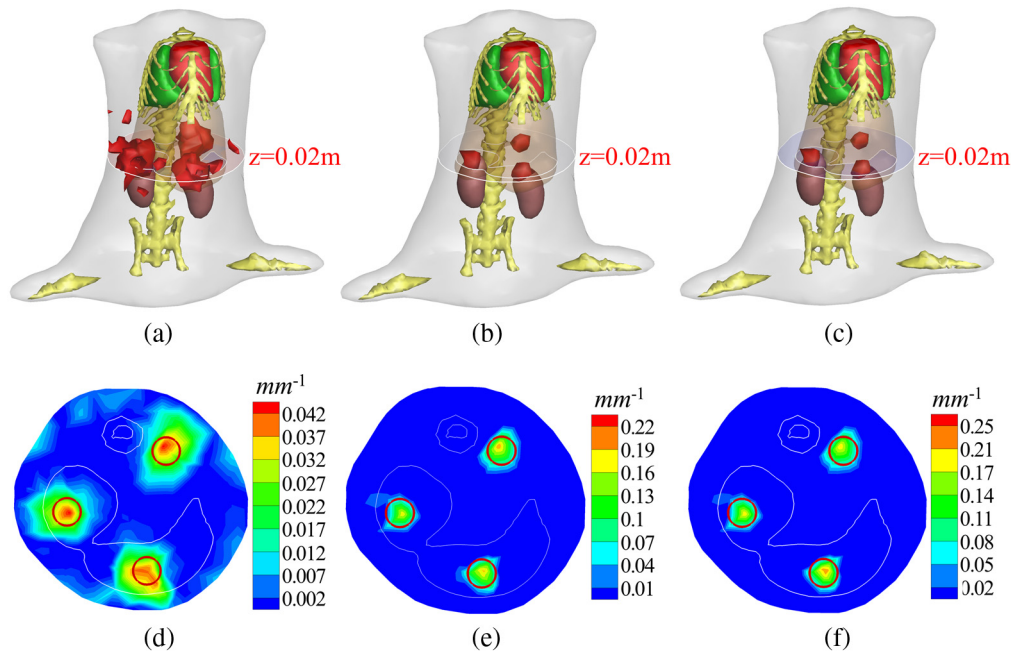


Fig. 2 Reconstruction results from the conjugate gradient based method with the l_2 -norm (CG_L2) [(a) and (d)], the iterated shrinkage based method with l_1 -norm (IS_L1) [(b) and (e)], and the proposed method [(c) and (f)] for three fluorescent sources and 12 measurement data sets: (a) to (c) The 3-D views of the reconstruction results. (d) to (f) The slice images in the $z = 0.02$ m plane. The red circles in the slice images denote the real positions of the fluorescent sources.

Table 2 Quantitative comparisons between the reconstruction results from the conjugate gradient based method with the l_2 -norm (CG_L2), the iterated shrinkage based method with l_1 -norm (IS_L1), and the proposed method for 12 measurement data sets corrupted by 5% Gaussian noise.

Source no.	PE (mm) (CG_L2)	PE (mm) (IS_L1)	PE (mm) (NSPGP)	RIE (%) (CG_L2)	RIE (%) (IS_L1)	RIE (%) (NSPGP)
S1	0.834	0.321	0.321	85.58	40.09	32.71
S2	0.733	0.690	0.690	85.82	25.15	12.33
S3	0.989	0.571	0.571	85.65	33.85	32.72

PE, position error; NSPGP, nonmonotone spectral projected gradient pursuit; RIE, relative intensity error.

the fluorescent sources with limited measurement data sets by using an appropriate reconstruction method. Here, only the measurement data sets generated by excitation point source 1, 5, and 9 were collected, as shown in Fig. 1(b). That is, only three measurement data sets corrupted by 5% Gaussian noise were used to reconstruct the fluorescent sources. The reconstructed results by the CG_L2 method, the IS_L1 method, and the proposed method are demonstrated in Fig. 3. The PEs of the reconstruction results, as well as the RIEs, are summarized in Table 3.

As shown in Fig. 3 and Table 3, when the measurement data were very limited and multiple fluorescent sources existed, the results reconstructed by the CG_L2 method were unacceptable. The PEs for the reconstructed sources S1 and S2 by the CG_L2 method were 1.872 and 1.792 mm, which were much bigger than those of the proposed method. The IS_L1 method was able to obtain satisfactory source localizations for the fluorescent sources S1 and S3, but the reconstructed fluorescent source S2 was not accurately located in the right regions. In contrast, the proposed method was able to recover all three fluorescent

sources accurately. Furthermore, the RIEs for the proposed method were smaller than those for the other two compared methods, which means that the fluorescence reconstructed by the proposed method had higher contrasts to the background compared to the other two methods. According to the above results, the proposed method was robust to limited measurement data and was able to obtain satisfactory results even in a badly ill-posed situation.

3.4 Evaluation of Reconstruction Efficiency

The high efficiency of the proposed method was also investigated. The CG_L2 method and the IS_L1 method were applied once again to reconstruct the same data sets in contrast to the proposed method. This experiment was conducted using the heterogeneous mouse model with three fluorescent sources, as shown in Fig. 1. To better evaluate the time-efficiency of the proposed method, we adopted five kinds of volumetric meshes with varying sizes to solve the FMT problem. For all three methods, the zero vector was used to initialize the

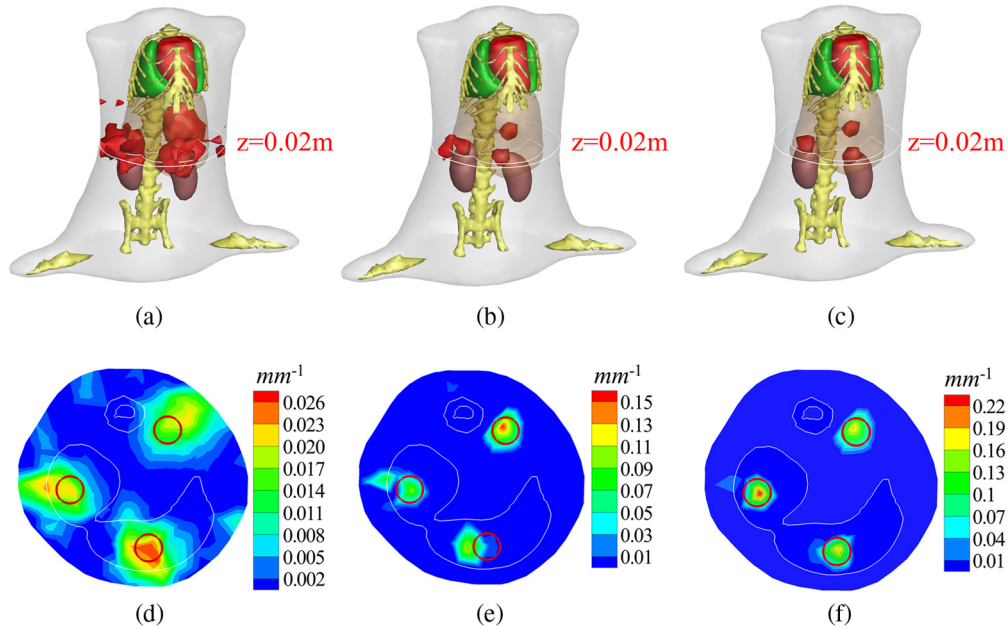


Fig. 3 Reconstruction results from the CG_L2 method [(a) and (d)], the IS_L1 method [(b) and (e)], and the proposed method for three fluorescent sources and three measurement data sets corrupted by 5% Gaussian noise. (a) to (c) The 3-D views of the reconstruction results. (d) to (f) The slice images in the $z = 0.02$ m plane. The red circles in the slice images denote the real positions of the fluorescent sources.

Table 3 Quantitative comparisons between the reconstruction results from the CG_L2 method, the IS_L1 method, and the proposed method for three measurement data sets corrupted by 5% Gaussian noise.

Source no.	PE (mm) (CG_L2)	PE (mm) (IS_L1)	PE (mm) (NSPGP)	RIE (%) (CG_L2)	RIE (%) (IS_L1)	RIE (%) (NSPGP)
S1	1.872	0.321	0.321	92.28	66.15	23.53
S2	0.733	1.907	0.690	90.68	56.57	27.54
S3	1.792	0.571	0.571	92.54	49.06	36.52

unknowns. Based on the different volumetric meshes, the reconstruction efficiency of the three methods was summarized in Table 4, which shows the time consumed by the three different methods for reconstruction of the five groups of data sets whose sizes were determined by the density of the discrete volumetric mesh. Each value of the reconstruction time in Table 4 was the average of 10 independent runs. Figure 4 demonstrates the comparison curves of reconstruction time of different methods.

Table 4 The comparison of the reconstruction efficiency based on different methods.

No.	Volumetric mesh size	CG_L2	IS_L1	NSPGP
1	2127 × 9807	57.44 s	41.69 s	4.25 s
2	2923 × 13,802	91.484 s	63.88 s	6.27 s
3	3563 × 17,058	155.784 s	92.06 s	8.33 s
4	4357 × 21,094	261.69 s	123.69 s	11.23 s
5	5220 × 25,603	436.09 s	172.55 s	14.77 s

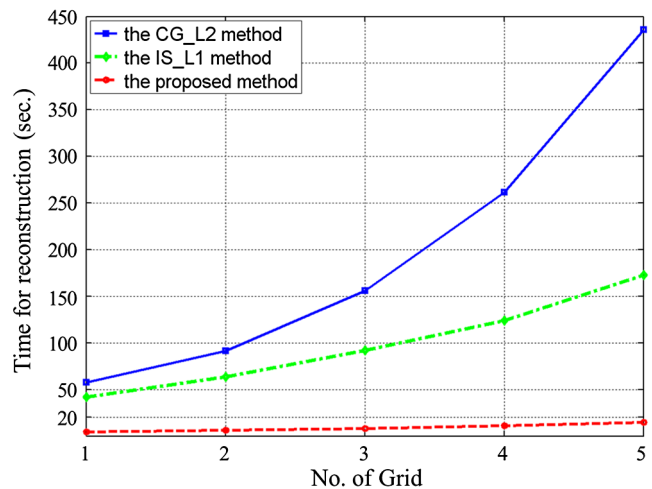


Fig. 4 Time cost comparisons among the CG_L2 method, the IS_L1 method, and the proposed method. The reconstruction time of the proposed method grows much more slowly than the two contrasting methods.

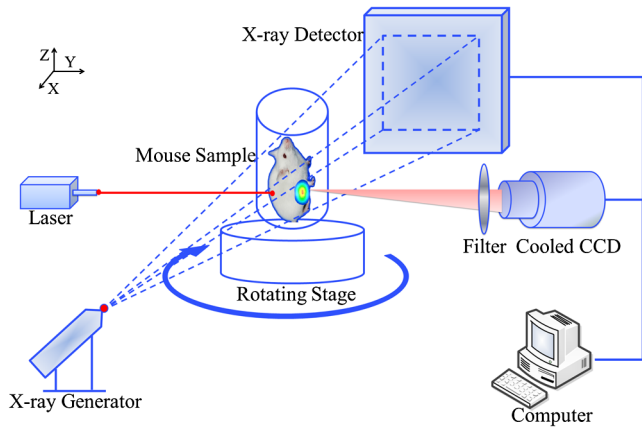


Fig. 5 The schematic illustration of the dual-modality imaging system.

The experimental results indicated the following. (1) When reconstructing the same data set, the IS_L1 method was more efficient than the CG_L2 method, but was less efficient than the proposed method. (2) When the size of the data set increased, the proposed NSPGP method became more computationally competitive, which is clearly depicted in Fig. 4. (3) All of the five data sets were discretized based on the heterogeneous mouse model with three fluorescent sources in the tissues of the

liver and muscle, indicating that the proposed method has the potential for practical FMT applications.

3.5 Practical Application

To validate the feasibility of the proposed method in the practical application of FMT, an *in vivo* mouse experiment was conducted. In this experiment, a nude mouse was utilized after it was implanted with a plastic fluorescent bead in the muscle. The fluorescent bead was filled with cy5.5 solution, which has an extinction coefficient of $\sim 0.019 \text{ mm}^{-1} \mu\text{M}^{-1}$ and a quantum efficiency of 0.23 at the peak excitation wavelength of 671 nm.⁴² The experiment was conducted using the dual-modality optical/x-ray CT imaging system developed by our group, which was an integrative platform that combines fluorescence imaging with x-ray CT scanning.^{38,43} The schematic illustration of the dual-modality imaging system is presented in Fig. 5, which is mainly equipped with a 671 nm continuous wave laser with an output power of 22 mW, along with an ultrasensitive cooled CCD camera with a $13 \mu\text{m} \times 13 \mu\text{m}$ pixel size, an x-ray generator, an x-ray detector, a rotating stage, and a set of optical lenses.

Before optical and x-ray data acquisition, the mouse was anesthetized and the fluorescent bead with cy5.5 solution was implanted stereotactically into the interspaces in the vicinity of the liver. The whole process to implement the proposed method for FMT reconstruction is depicted by Fig. 6. The optical data

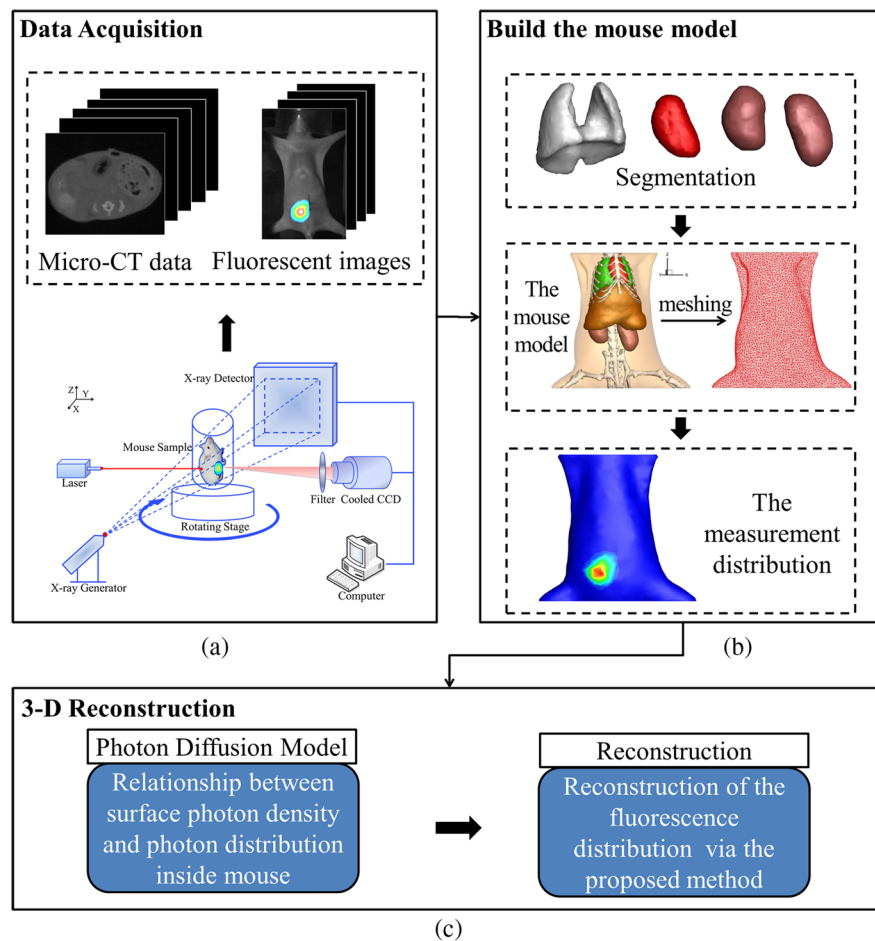


Fig. 6 Method overview. (a) optical and x-ray data acquisition. (b) building the heterogeneous mouse model. (c) reconstruction of the fluorescent distribution in the mouse model. l_1 -norm optimization.

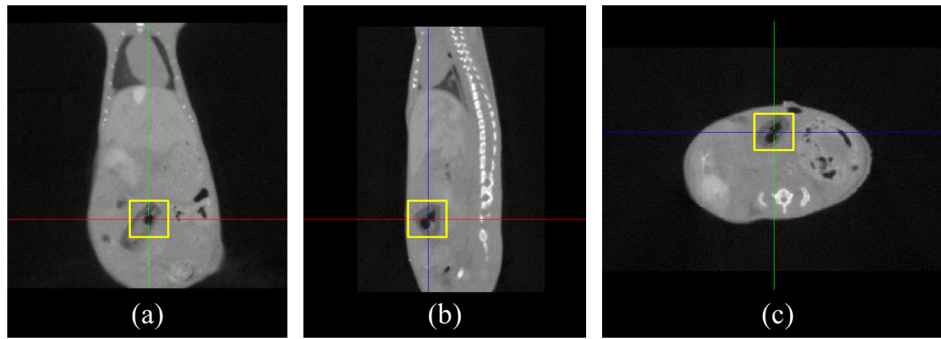


Fig. 7 Three slices of the micro-CT mouse data, where the yellow square marks the location of the fluorescent bead: (a) the coronal view, (b) the sagittal view, and (c) the transversal view.

were acquired first. Fluorescent images from four views were collected from the mouse surface. After the acquisition of the optical data, the mouse was scanned using micro-CT to obtain the anatomical structure, as shown in Fig. 6(a). The fluorescent bead can be distinguished in the CT images, as shown in Fig. 7, where the yellow square marks the location of the fluorescent bead at the coordinates (52.83, 52.91, 13.00).

Data processing followed data acquisition. First, the mouse structural data were reconstructed by the GPU accelerated Feldkamp-Davis-Kress algorithm.³⁷ Then the major organs and tissues were segmented to build the heterogeneous mouse model. The optical properties for the mouse organs and tissues were calculated based on Alexandrakis et al.'s work⁴⁴ as listed in Table 5. Next, the mouse torso was discretized into a volumetric mesh which contains 4667 nodes and 24,451 tetrahedral elements. The mouse torso utilized for FMT reconstruction covered

over 60% of the volume of the mouse body. Finally, in order to portray the photon distribution on the surface of the mouse torso, the fluorescent images were mapped onto the surface of the volumetric mesh in the light of space and energy, as shown in Fig. 6(b). The surface energy mapping was conducted using a 3-D surface flux reconstruction method.⁴⁵

After the above procedures, the reconstruction of the fluorescent distribution inside the mouse was conducted. Figure 8 shows the results reconstructed by the CG_L2 method, the IS_L1 method, and the proposed method. The muscle region was set to be translucent so that the reconstructed fluorescent source was not covered. Quantitative comparisons of the results for the above three methods are presented in Fig. 9 and Table 6. It can be perceived that the fluorescent source reconstructed by the CG_L2 method was widely scattered and could not be accurately localized with a location error of 2.84 mm. The IS_L1

Table 5 Optical properties of the mouse organs and tissues.

Material	Muscle (mm^{-1})	Lungs (mm^{-1})	Heart (mm^{-1})	Liver (mm^{-1})	Kidneys (mm^{-1})	Bone (mm^{-1})
μ_{ax}	0.0849	0.1918	0.0574	0.3437	0.0644	0.0593
μ'_{sx}	0.4273	2.1720	0.9620	0.6770	2.2480	2.4900
μ_{am}	0.0563	0.1266	0.383	0.2283	0.0430	0.0393
μ'_{sm}	0.3792	2.1240	0.9050	0.6480	2.1090	2.3400

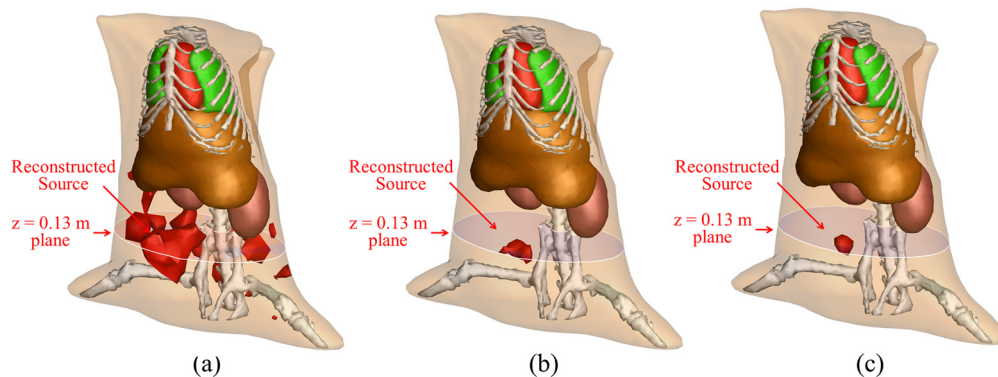


Fig. 8 The isosurface 3-D views of the results reconstructed by the CG_L2 method, the IS_L1 method, and the proposed method. (a) The reconstruction results by the CG_L2 method. (b) The reconstruction results by the IS_L1 method. (c) The reconstruction results by the proposed method.

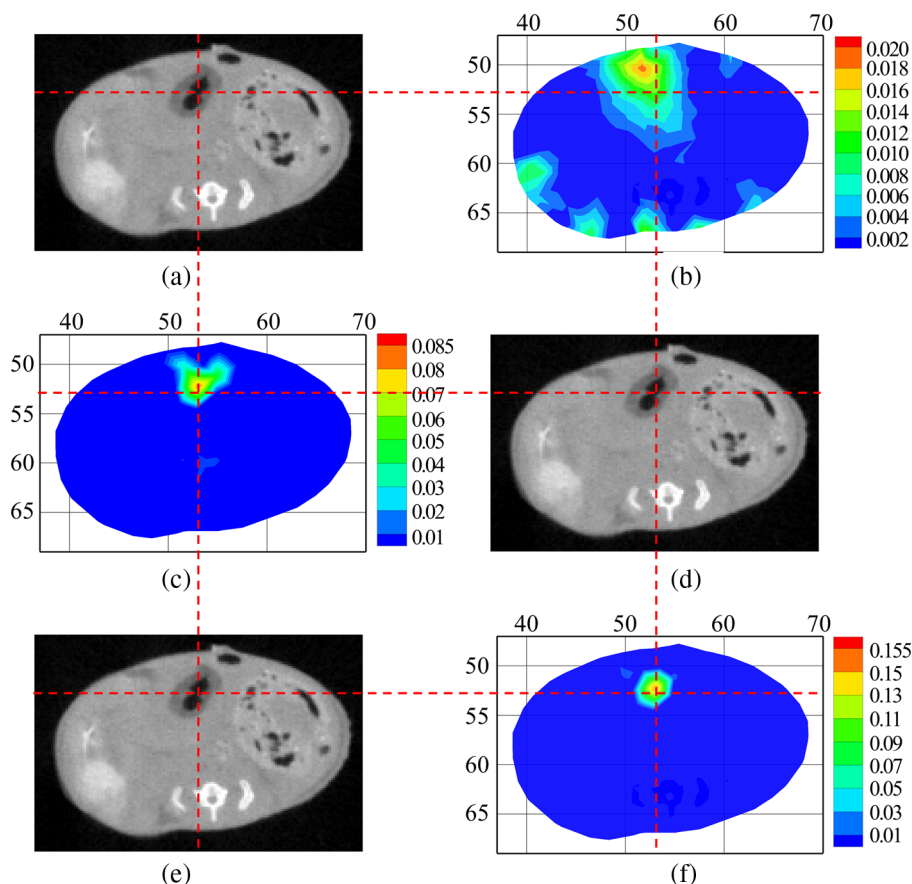


Fig. 9 The comparisons of the reconstruction results for *in vivo* mouse studies. (a), (d), and (e) Transverse views of the CT slices, where the home-made fluorescent bead can be observed in the CT slices. (b), (c), and (f) Two-dimensional views of the reconstruction results, whose slice selections are the same as (b), (c), and (f).

Table 6 Comparisons of the reconstruction results among different methods.

Method	Actual position center (mm)	Reconstructed position center (mm)	Position error (mm)	Reconstruction time (s)
CG_L2	(52.83, 52.91, 13.00)	(51.70, 50.30, 12.98)	2.84	82.70
IS_L1	(52.83, 52.91, 13.00)	(53.07, 52.24, 12.67)	0.78	49.08
Proposed	(52.83, 52.91, 13.00)	(53.07, 52.24, 12.67)	0.78	4.11

method and the proposed method were both able to obtain satisfactory reconstruction results with a position error of only 0.78 mm. However, the results of the proposed method were better than those of the IS_L1 method because the fluorescent source reconstructed by the proposed method was more concentrated and did not have any artifacts. Besides, the fluorescence reconstructed by the proposed method had a higher contrast to the background. The reconstruction time of the proposed method was 4.14 s and was about one order of magnitude faster than the two contrasting methods, which demonstrated the absolute advantages of the proposed method in efficiency.

The above results reveal that the proposed method was able to reconstruct the fluorescent source accurately and had the potential to detect the lesions for practical biomedical applications.

4 Conclusion

In this paper, a novel method based on nonmonotone spectral projected gradient pursuit with l_1 -norm has been proposed to localize the internal fluorescent sources. At each iteration, a spectral projected gradient method approximately minimizes a least-squares problem with an explicit one-norm constraint. A nonmonotone line search strategy is introduced to get the appropriate updating direction. This strategy can overcome the case where the sequence of iterates follows the bottom of a curved narrow valley, thus guaranteeing the global convergence. The Barzilai–Borwein step length is adopted to build the optimal step length at each iteration, which requires little computational work and can accelerate the convergence process. In order to generate a more precise photon diffusion model for

fluorescent source reconstruction, structure priors have been utilized to assemble a heterogeneous mouse model by extracting the major organs and tissues of the mouse. To evaluate the performance of the proposed method, three numerical simulation experiments and one *in vivo* mouse experiment have been conducted.

The experimental results suggest the following. (1) The proposed NSPGP method is capable of guaranteeing the reconstruction accuracy for FMT, and it is able to localize different fluorescent sources with a position bias <1 mm. (2) It maintains stable fluorescent source reconstruction results even under quite ill-posed conditions, where the measurement data sets are quite limited. (3) Regarding the same measurement data sets, the proposed method is more efficient compared to the classical iterated shrinkage based method and the conjugate gradient based method, especially for the high-dimensional problems in fluorescent source reconstruction. (4) The potential of the proposed method on the practical application of FMT has also been validated further by the *in vivo* experiment on a nude mouse model, in which a small fluorescent source located in the vicinity of the liver is accurately reconstructed.

Although the proposed NSPGP method has achieved promising results, some practical applications in FMT are still very challenging. Future work will focus on the study for more practical applications, e.g., to conduct *in vivo* experiments based on probe-marked mouse models to determine if our method is able to reconstruct the weak light signals of tumors. Additionally, the *in vivo* experiment could be extended further to detect the weak optical signals from the internal fluorescent sources at different depths in the mouse. We believe that FMT will provide more potential for early detection of tumors and evaluation of treatment with rapid development of the reconstruction methods.

Acknowledgments

This paper is supported by the National Basic Research Program of China (973 Program) under Grant No. 2011CB707700, the National Natural Science Foundation of China under Grant No. 81227901 and 61231004, the National Key Technology R&D Program of China under Grant No. 2012BAI23B01, and the Instrument Developing Project of the Chinese Academy of Sciences under Grant No. YZ201359. The authors thank adjunct assistant professor Dr. Karen M. von Deneen from the University of Florida for her modifications in this paper.

References

1. V. Ntziachristos, "Going deeper than microscopy: the optical imaging frontier in biology," *Nat. Methods* **7**(8), 603–614 (2010).
2. F. G. Blankenberg and H. W. Strauss, "Recent advances in the molecular imaging of programmed cell death: Part II—non-probe-based MRI, ultrasound, and optical clinical imaging techniques," *J. Nucl. Med.* **54**(1), 1–4 (2013).
3. S. Keereweer et al., "Optical image-guided surgery—where do we stand?," *Mol. Imaging Biol.* **13**(2), 199–207 (2011).
4. T. F. Massoud and S. S. Gambhir, "Molecular imaging in living subjects: seeing fundamental biological processes in a new light," *Genes Dev.* **17**(5), 545–580 (2003).
5. V. Ntziachristos, "Fluorescence molecular imaging," *Annu. Rev. Biomed. Eng.* **8**, 1–33 (2006).
6. A. Ale et al., "FMT-XCT: *in vivo* animal studies with hybrid fluorescence molecular tomography-X-ray computed tomography," *Nat. Methods* **9**(6), 615–620 (2012).
7. A. X. Cong and G. Wang, "A finite-element-based reconstruction method for 3D fluorescence tomography," *Opt. Express* **13**(24), 9847–9857 (2005).
8. Q. Zhao et al., "A handheld fluorescence molecular tomography system for intraoperative optical imaging of tumor margins," *Med. Phys.* **38**(11), 5873–5878 (2011).
9. X. L. Song et al., "Reconstruction for free-space fluorescence tomography using a novel hybrid adaptive finite element algorithm," *Opt. Express* **15**(26), 18300–18317 (2007).
10. N. Deliolanis et al., "Free-space fluorescence molecular tomography utilizing 360 geometry projections," *Opt. Lett.* **32**(4), 382–384 (2007).
11. D. F. Wang, X. L. Song, and J. Bai, "Adaptive-mesh-based algorithm for fluorescence molecular tomography using an analytical solution," *Opt. Express* **15**(15), 9722–9730 (2007).
12. W. Bangerth and A. Joshi, "Adaptive finite element methods for the solution of inverse problems in optical tomography," *Inverse Probl.* **24**(3), 034011 (2008).
13. F. H. Tian et al., "Enhanced functional brain imaging by using adaptive filtering and a depth compensation algorithm in diffuse optical tomography," *IEEE Trans. Med. Imaging* **30**(6), 1239–1251 (2011).
14. L. Z. Xiang et al., "4-D photoacoustic tomography," *Sci. Rep.* **3**, 1113 (2013).
15. Y. J. Lu et al., "Source reconstruction for spectrally-resolved bioluminescence tomography with sparse a priori information," *Opt. Express* **17**(10), 8062–8080 (2009).
16. M. A. Figueiredo, R. D. Nowak, and S. J. Wright, "Gradient projection for sparse reconstruction: application to compressed sensing and other inverse problems," *IEEE Sel. Topics Signal Process.* **1**(4), 586–597 (2007).
17. M. Lustig, D. Donoho, and J. M. Pauly, "Sparse MRI: the application of compressed sensing for rapid MR imaging," *Magn. Reson. Med.* **58**(6), 1182–1195 (2007).
18. D. L. Donoho, "Compressed sensing," *IEEE Trans. Inf. Theory* **52**(4), 1289–1306 (2006).
19. E. J. Candès, J. Romberg, and T. Tao, "Robust uncertainty principles: exact signal reconstruction from highly incomplete frequency information," *IEEE Trans. Inf. Theory* **52**(2), 489–509 (2006).
20. P. Mohajerani et al., "Optimal sparse solution for fluorescent diffuse optical tomography: theory and phantom experimental results," *Appl. Opt.* **46**(10), 1679–1685 (2007).
21. N. Cao, A. Nehorai, and M. Jacob, "Image reconstruction for diffuse optical tomography using sparsity regularization and expectation-maximization algorithm," *Opt. Express* **15**(21), 13695–13708 (2007).
22. D. Han et al., "Sparsity-promoting tomographic fluorescence imaging with simplified spherical harmonics approximation," *IEEE Trans. Biomed. Eng.* **57**(10), 2564–2567 (2010).
23. D. Han et al., "A fast reconstruction algorithm for fluorescence molecular tomography with sparsity regularization," *Opt. Express* **18**(8), 8630–8646 (2010).
24. J. Shi et al., "Efficient L1 regularization-based reconstruction for fluorescent molecular tomography using restarted nonlinear conjugate gradient," *Opt. Lett.* **38**(18), 3696–3699 (2013).
25. V. C. Kavuri et al., "Sparsity enhanced spatial resolution and depth localization in diffuse optical tomography," *Biomed. Opt. Express* **3**(5), 943–957 (2012).
26. J. Barzilai and J. M. Borwein, "Two-point step size gradient methods," *IMA J. Numer. Anal.* **8**(1), 141–148 (1988).
27. M. Raydan, "On the Barzilai and Borwein choice of steplength for the gradient-method," *IMA J. Numer. Anal.* **13**(3), 321–326 (1993).
28. Y. Y. Tan and H. B. Jiang, "DOT guided fluorescence molecular tomography of arbitrarily shaped objects," *Med. Phys.* **35**(12), 5703–5707 (2008).
29. A. Joshi, W. Bangerth, and E. M. Sevick-Muraca, "Adaptive finite element based tomography for fluorescence optical imaging in tissue," *Opt. Express* **12**(22), 5402–5417 (2004).
30. J. H. Lee, A. Joshi, and E. M. Sevick-Muraca, "Fully adaptive finite element based tomography using tetrahedral dual-meshing for fluorescence enhanced optical imaging in tissue," *Opt. Express* **15**(11), 6955–6975 (2007).
31. M. Schweiger et al., "The finite-element method for the propagation of light in scattering media—boundary and source conditions," *Med. Phys.* **22**(11), 1779–1792 (1995).
32. R. Tibshirani, "Regression shrinkage and selection via the lasso," *J. R. Stat. Soc. B* **58**(1), 267–288 (1996).

33. Y. Yu and L. Gao, "Nonmonotone line search algorithm for constrained minimax problems," *J. Optim. Theory Appl.* **115**(2), 419–446 (2002).
34. Y. Dai, "On the nonmonotone line search," *J. Optim. Theory Appl.* **112**(2), 315–330 (2002).
35. M. Raydan, "The Barzilai and Borwein gradient method for the large scale unconstrained minimization problem," *SIAM J. Optim.* **7**(1), 26–33 (1997).
36. C. Chen et al., "Diffuse optical tomography enhanced by clustered sparsity for functional brain imaging," *IEEE Trans. Med. Imaging*, **33**(12), 2323–2331 (2014).
37. G. Yan et al., "Fast cone-beam CT image reconstruction using GPU hardware," *J. X-Ray Sci. Technol.* **16**(4), 225–234 (2008).
38. S. Zhu et al., "Cone beam micro-CT system for small animal imaging and performance evaluation," *J. Biomed. Imaging* **2009**, 960573 (2009).
39. H. Yi et al., "Reconstruction algorithms based on l_1 -norm and l_2 -norm for two imaging models of fluorescence molecular tomography: a comparative study," *J. Biomed. Opt.* **18**(5), 56013 (2013).
40. A. B. Milstein et al., "Fluorescence optical diffusion tomography using multiple-frequency data," *JOSA A* **21**(6), 1035–1049 (2004).
41. J. Nocedal and S. J. Wright, *Conjugate Gradient Methods*, Springer, New York (2006).
42. F. Gao et al., "A linear, featured-data scheme for image reconstruction in time-domain fluorescence molecular tomography," *Opt. Express* **14**(16), 7109–7124 (2006).
43. C. H. Qin, S. P. Zhu, and J. Tian, "New optical molecular imaging systems," *Curr. Pharm. Biotechnol.* **11**(6), 620–627 (2010).
44. G. Alexandrakis, F. R. Rannou, and A. F. Chatziioannou, "Tomographic bioluminescence imaging by use of a combined optical-PET (OPET) system: a computer simulation feasibility study," *Phys. Med. Biol.* **50**(17), 4225 (2005).
45. X. Chen et al., "3D reconstruction of light flux distribution on arbitrary surfaces from 2D multi-photographic images," *Opt. Express* **18**(19), 19876–19893 (2010).

Jinzuo Ye is currently a postgraduate student with the Key Laboratory of Molecular Imaging of the Chinese Academy of Sciences, Institute of Automation, Chinese Academy of Sciences, Beijing, China. He received his BS degree in software engineering from Nankai University in 2011 and his MS degree in computer technology from the Institute of Automation, Chinese Academy of Sciences in 2014. His main research interests include multimodality molecular imaging and fluorescence molecular tomography.

Yang Du is currently an associate professor with the Key Laboratory of Molecular Imaging of the Chinese Academy of Sciences, Institute of Automation, Chinese Academy of Sciences, Beijing, China. Her research interests are concentrated on the mechanism of tumor genesis and progress.

Yu An is currently a postgraduate student with the Beijing Jiaotong University School of Computer and Information Technology. His research interests include optical molecular imaging and medical image processing.

Chongwei Chi is currently an assistant professor with the Key Laboratory of Molecular Imaging of the Chinese Academy of Sciences, Institute of Automation, Chinese Academy of Sciences, Beijing, China. His main research interests are focused on biomedical imaging.

Jie Tian is a professor and director of the Key Laboratory of Molecular Imaging of the Chinese Academy of Sciences, Institute of Automation, Chinese Academy of Sciences, Beijing, China. His current research interests include medical image process and analysis, and pattern recognition. He has authored or coauthored more than 100 research papers in international journals and conferences.